LUND UNIVERSITY

Predicting the formation of different tissue types during Achilles tendon healing using mechanoregulated and oxygen-regulated frameworks

Notermans, Thomas; Isaksson, Hanna

Predicting the formation of different tissue types during Achilles tendon healing using mechano-regulated and oxygen-regulated frameworks

Thomas Notermans[1*] , Hanna Isaksson[1]

[1]Department of Biomedical Engineering, Lund University, Lund, Sweden

ORCID: Thomas Notermans: 0000-0003-0381-3616; Hanna Isaksson: 0000-0002-9690-8907

[*]Corresponding author: E-mail: thomas.notermans@bme.lth.se

Keywords: mechanobiology – angiogenesis – endochondral ossification – heterotopic ossification – cell infiltration

Abstract

During Achilles tendon healing in rodents, besides the expected tendon tissue, also cartilage-, bone- and fat-like tissue features have been observed during the first twenty weeks of healing. Several studies have hypothesized that mechanical loading may play a key role in the formation of different tissue types during healing. We recently developed a computational mechanobiological framework to predict tendon tissue production, organization and mechanical properties during tendon healing. In the current study, we aimed to explore possible mechanobiological related mechanisms underlying formation of other tissue types than tendon tissue during tendon healing. To achieve this, we further developed our recent framework to predict formation of different tissue types, based on mechanobiological models established in other fields, which have earlier not been applied to study tendon healing. We explored a wide range of biophysical stimuli, i.e. principal strain, hydrostatic stress, pore pressure, octahedral shear strain, fluid flow, angiogenesis and oxygen concentration, that may promote the formation of different tissue types. The numerical framework predicted spatio-temporal formation of tendon-, cartilage-, bone- and to a lesser degree fat-like tissue throughout the first twenty weeks of healing, similar to recent experimental reports. Specific features of experimental data were captured by different biophysical stimuli. Our modeling approach showed that mechanobiology may play a role in governing the formation of different tissue types that have been experimentally observed during tendon healing. This study provides a numerical tool that can contribute to a better understanding of tendon mechanobiology during healing. Developing these tools can ultimately lead to development of better rehabilitation regimens that stimulate tendon healing and prevent unwanted formation of cartilage-, fat- and bone-like tissues.

1. Introduction

The incidence of Achilles tendon rupture has been increasing throughout the last decades (Ganestam et al. 2016; Huttunen et al. 2014; Lemme et al. 2018; Nyyssönen et al. 2008). The rehabilitation regimen after rupture could play a key role for the healing outcome (Holm et al. 2015), where e.g. different mechanical loading regimens have been found to affect the outcome in humans (El-Akkawi et al. 2018; Ochen et al. 2019). To design loading protocols that better stimulate tendon healing, there is a need to understand tendon mechanobiology, i.e. the adaptation of tendon properties to external mechanical loading. To study this, small animal models are most commonly used (Notermans et al. 2021a). Recent experimental studies in rodents have reported significant aberrant formation of tissues other than tendon-tissue, e.g. formation of fat- (Huber et al. 2020; Khayyeri et al. 2020), cartilage- (Asai et al. 2014; da Silva et al. 2020; Howell et al. 2017; Khayyeri et al. 2020; Korntner et al. 2017; Misir et al. 2019) or bone-like tissue features (Asai et al. 2014; Chen et al. 2017; Hsieh et al. 2016; Huber et al. 2020; Lin et al. 2010; Sakabe et al. 2018; Zhang et al. 2016) (Fig 1). These studies showed that areas of cartilage-like tissue could be identified after between four and 17 weeks of healing, whereas bone-like tissue was present from five up to 16 weeks of healing (Lin et al. 2010) (Fig 1). Particularly, the long-term studies showed that bone-like tissue may take up a large volume of the healing tendon at the later time points (Hsieh et al. 2016; Sakabe et al. 2018).

Several studies have found fat-, cartilage- (Khayyeri et al. 2020) and bone-like cells (Lin et al. 2010) throughout early healing. In particular, chondrocyte-like cells were identified already in the first weeks of healing (Asai et al. 2014; da Silva et al. 2020; Khayyeri et al. 2020). Asai et al. (2014) found cartilage-like cells (round cells) between two to four weeks, they observed cartilage-specific matrix proteins (collagen type 2 and aggrecan) at eight weeks, and they found

71   bone-like tissue at 12 weeks in all rat Achilles tendons in their study using CT imaging. Santos

72   Da Silva et al. (2020) also observed progressive production of collagen type 2 throughout 17

73   weeks of healing, and chondrocyte-like cells were still present around islands of mineralized

74   tissue at 17 weeks. Howell et al. (2017) hypothesized that tenocytes (intrinsic tendon cells)

75   contribute to cartilage formation in the tendon stumps and that this may be a key factor why the

76   tendon heals poorly. Another study pointed out that cartilage could facilitate bone formation

77   through the endochondral pathway (Lin et al. 2010). They showed that an initial chondrogenic

78   phase was followed by bone formation, which started between three and five weeks of healing.

79   The chondrogenic phase also displayed high expression of hypoxia-inducible factor 1α,

80   whereas the bone formation phase displayed high vascular endothelial growth factor

81   expression. This indicates that cartilage formation may occur during hypoxic-conditions,

82   whereas bone formation typically occurs in presence of blood vessels (providing sufficient

83   oxygen). This complies well with what is known from other regenerative situations in

84   experimental (e.g. (Buckley et al. 2010; Hausman et al. 2001; Hirao et al. 2006)) and numerical

85   studies (e.g. (Burke and Kelly 2012; Checa et al. 2010; Geris et al. 2008)). Another study in

86   rotator cuff tendons, showed that calcifications were surrounded by blood vessels (Darrieutort-

87   Laffite et al. 2019), confirming that angiogenesis and oxygen levels play important roles in

88   bone-like tissue formation in tendons as well.

89

Cartilage-like (Histology) | **Bone-like (X-rays, CT)**

W4 | W8 | W15 | W16

Howell et al., 2017 | Howell et al., 2017 | Sakabe et al., 2018 | Hsieh et al., 2016
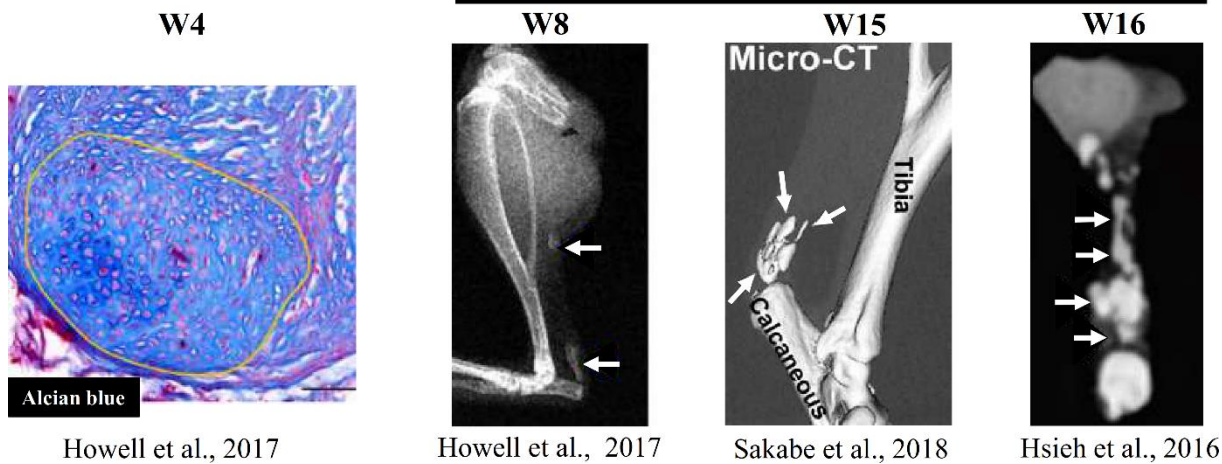
Fig 1 Examples of literature evidence that tendon healing involves formation of cartilage-like and bone-like tissues . The circled area in the histological section (left) with Alcian blue depicts cartilage deposition and cell morphology. The X-ray and CT images (right) depict the high-density bone-like tissue formation (white arrows). Images were collected from the following references (Howell et al. 2017; Hsieh et al. 2016; Sakabe et al. 2018), reused under the Creative Commons CC-BY and Creative Commons Attribution license 4.0. More literature examples of cartilage-like and bone-like tissue formations throughout 17 weeks of healing in rat Achilles tendon can be found in: (Asai et al. 2014; da Silva et al. 2020; Howell et al. 2017; Hsieh et al. 2016; Huber et al. 2020; Lin et al. 2010; Misir et al. 2019; Sakabe et al. 2018).

Mechanobiological review articles on tendon healing mentioned that mechanical loading, in particular over- and unloading, may cause aberrant tissue formation (Freedman et al. 2015; Notermans et al. 2021a). It has been reported that the level of bone-like tissue formation during healing depends on the level of loading on the tendon. Recently, Huber et al. (2020) showed that joint immobilization could limit bone-like tissue formation (Huber et al. 2020). The authors proposed that joint immobilization was associated with decreased collagen organization, cell spreading and transcriptional activator with PDZ-binding domain (TAZ) signaling, thereby

108 inducing adipocyte differentiation. Oppositely, they proposed that fiber alignment, cell

109 spreading and TAZ signaling increases upon loading, inducing ectopic bone formation. The

110 bone-like tissue volume after six weeks of healing was highest for the loaded tendon

111 experiencing free cage activity (Huber et al. 2020). However, partial immobilization decreased

112 the amount of fibrocartilage (Palmes et al. 2002) and bone-like tissue volume (Chen et al. 2017),

113 compared to full immobilization.

114

115 Although experimental evidence is accumulating, there is no computational framework to date

116 that has investigated mechanoregulated tissue differentiation or the formation of different tissue

117 types during tendon healing. However, there is a range of numerical algorithms available that

118 investigated the role of mechanical loading during bone regeneration (Burke and Kelly 2012;

119 Carter et al. 1998; Checa et al. 2010; Claes and Heigele 1999; Isaksson et al. 2008; Lacroix and

120 Prendergast 2002). A wide range of biophysical stimuli has been explored, i.e. principal or

121 octahedral shear strain, pore pressure, hydrostatic stress or fluid flow, in terms of its ability to

122 regulate cell differentiation and subsequent formation of different tissue types, e.g. cartilage,

123 (im)mature bone, bone marrow, granulation tissue, fibrous tissue (Isaksson et al. 2008; Isaksson

124 et al. 2006b). These finite element frameworks were later expanded, for example, by

125 investigating the role of mechano-regulated angiogenesis, local tissue stiffness and oxygen

126 concentration in terms of its effect on tissue differentiation during bone healing (Burke and

127 Kelly 2012).

128

129 We recently developed a mechanobiological tendon healing framework that incorporates

130 mechanical and cellular regulatory mechanisms to predict spatial and temporal tendon tissue

131 production, organization and mechanical properties (Notermans et al. 2021b) (Notermans et al.

2021c). In the current study, we aimed to explore possible mechanobiological mechanisms underlying the formation of other tissue types during tendon healing. To investigate this, we further developed our recent framework (Notermans et al. 2021b) (Notermans et al. 2021c) to include predictions of tissue differentiation and subsequent formation of different tissue types, based on knowledge from the field of bone regeneration (Burke and Kelly 2012; Carter et al. 1998; Claes and Heigele 1999; Isaksson et al. 2006b; Lacroix and Prendergast 2002). The presented framework is able to capture heterogeneous production of tendon-, cartilage- and bone-like tissues throughout tendon healing. The predictions are compared to qualitative observations in recent experimental studies.

2. Methods

We recently developed a mechanobiological framework that allows us to predict tendon tissue formation and reorientation in response to mechanical stimulation (Notermans et al. 2021b) (Notermans et al. 2021c, Journal of Biomechanics – in press). Briefly, a 3D finite element model for tendon healing was combined with an existing fibre-reinforced hyper-visco-poro-elastic material model tendon (Khayyeri et al. 2016; Notermans et al. 2019). An iterative framework (Fig 2) was implemented to predict spatial and temporal tissue production, collagen reorientation, and the temporal evolution of mechanical properties in the healing tendon callus (see more details in (Notermans et al. 2021b) (Notermans et al. 2021c, Journal of Biomechanics – in press)). This was used as a starting point in the current study. In the current study, the tendon was stimulated with a mechanical load during every iteration of healing and subsequently tendon-, cartilage-, bone- or fat-like tissue were predicted to form in the healing callus, depending on a range of different biophysical stimuli (Table 1). In addition, the process

155 of endochondral bone formation was explored, and a parameter sensitivity analysis of the

156 angiogenesis and oxygen-dependent framework was performed.
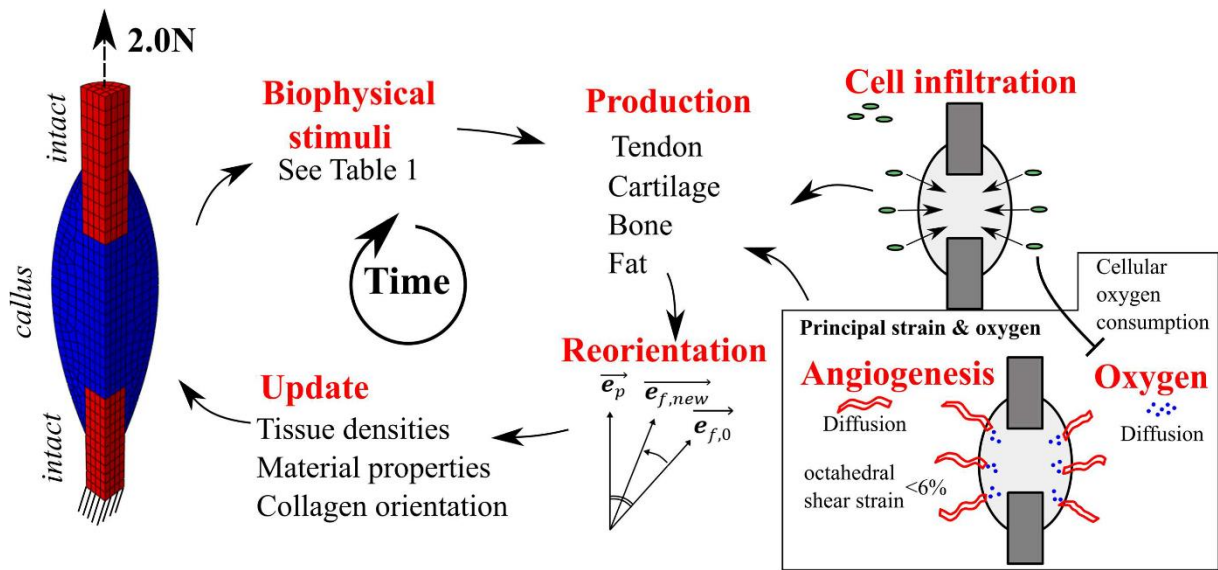
157

158 **Fig 2** *Overview of the iterative framework to predict formation of different tissue types during*

159 *tendon healing. A 2N mechanical load was applied to the FE model and a wide range of*

160 *biophysical stimuli were calculated according to existing tissue differentiation algorithms (see*

161 *Table 1) to predict formation of tendon-, cartilage-, bone- and fat-like tissues. Diffusion*

162 *simulations were utilized to model cell infiltration, angiogenesis and oxygen diffusion, where*

163 *oxygen was consumed by cells.*

164

165 **2.1 The Finite Element Model**

166 A finite element (FE) mesh was created based on geometrical measurements from healing rat

167 Achilles tendon that had been subjected to 1 week of free cage activity after rupture (details on

168 geometry and boundary conditions are available in Online Resource 1 and 2) (Khayyeri et al.

169 2020). The healing tendon consisted of two stumps with aligned collagen fibres (one direction,

170 anisotropic), and a bulging healing callus with 13 collagen fiber directions (simulating random

171 orientation) in every material point. The densities of collagen and ground matrix in the callus

172   were set to 10% (compared to stumps) at the start of healing. The FE model was subjected to

173   2.0 N tensile load, representing the maximum force during gait in adult female Sprague-Dawley

174   rats (Song et al. 2019). Mechanical loading was applied as a linear ramp at a rate of 1.1 N/s. All

175   simulations were performed in Abaqus v2017 (Dassault Systèmes Simulia Corp., Johnston, RI,

176   USA).

177

178   **2.2 Mechanoregulatory schemes**

179   Mechanoregulatory algorithms based on different biophysical stimuli were used to predict the

180   tissue formation of tendon-, fat-, cartilage- and bone-like tissue (Table 1). Several existing

181   mechanoregulatory schemes were adopted and investigated (Carter et al. 1998; Claes and

182   Heigele 1999; Lacroix and Prendergast 2002). These algorithms utilize hydrostatic stress (HS)

183   and octahedral shear strains (OSS) that were calculated according to:

184    $$\sigma_{hydrostatic} = \frac{tr(\boldsymbol{\sigma})}{3} = \frac{(\sigma_1 + \sigma_2 + \sigma_3)}{3}$$

185    $$\varepsilon_{os} = \frac{1}{3}\sqrt{\left(\varepsilon_1 - \varepsilon_3\right)^2 + \left(\varepsilon_1 - \varepsilon_2\right)^2 + \left(\varepsilon_2 - \varepsilon_3\right)^2}$$

186   where hydrostatic stress ($\sigma_{hydrostatic}$) is defined as the trace of the stress tensor ($\boldsymbol{\sigma}$) in cartesian

187   format and octahedral shear strain (ε_{os}) depends on the maximum (ε_1), mid (ε_2) and minimum

188   (ε_3) principal strains. In addition to these existing algorithms, a new mechanoregulatory

189   scheme was designed using solely the (maximum) principal strain (PE) thresholds for predicting

190   cartilage- (2-4%) and bone-like tissue formation (<2%). Simulations of intact tendon were

191   performed to verify the validity of these thresholds (Online Resource 3). The same strain

192   thresholds were utilized in combination with the oxygen framework by Burke et al. (2012),

193   which was originally designed using local matrix stiffness instead of principal strain. A

194   principal strain threshold for fat (>25%) was added to the oxygen framework. The 3% oxygen

9

concentration and 90% angiogenesis threshold for cartilage- and bone-like tissue formation, respectively, were adopted from the study by Burke et al. (2012).

Stimuli:	Princ. strain	Princ. Strain & Hydro. stress	Princ. Strain & Pore pressure	Octa. shear strain & Fluid flow	Princ. Strain & Oxygen Angiogenesis
Model:	PE	PE-HS	PE-PP	OSS-FF	PE-OXY (A)
Reference:		(Carter et al. 1998)	(Claes and Heigele 1999)	(Lacroix and Prendergast 2002)	(Burke and Kelly 2012)
Tendon	>4*	>5; <0.2	>15; >0.15 >5; <-0.15 or >0.15	stim>3	-;3; <90* 2-25%; >3; >90*
Cartilage	2-4	<5; >0.2	<15; >0.15	1<stim<3	-;<3; -
Bone	<2	<5; <0.2	<5; <±0.15	stim>1	<2; -; >90
Fat	-	-	-	-	>25;-;>90

Table 1 *Overview of the biophysical thresholds implemented to predict formation of tendon, fat, cartilage- and bone-like tissues. Different biophysical stimuli, i.e. maximum principal strain (PE, %), hydrostatic stress (HS, MPa), pore pressure (PP, MPa), octahedral shear strain (OSS, %), fluid flow (FF, µm/s), oxygen concentration (OXY, %) and angiogenesis (A, %), were based on (Burke and Kelly 2012; Carter et al. 1998; Claes and Heigele 1999; Lacroix and Prendergast 2002). The octahedral shear strain and fluid flow algorithm is based on a general stimulus (stim) that is calculated according: stim = OSS/3.75 + FF/3 (Lacroix and Prendergast 2002). The (maximum) principal strain (PE) and principal strain with oxygen algorithms included tendon production (noted with asterisks) according to a strain magnitude-dependent production law (Online Resource 4) utilized in a previous study when predicting strain-dependent tendon formation (Notermans et al. 2021b) (Notermans et al. 2021c).*

2.3 Tissue production rates

210   The healing framework describing collagen production and reorientation laws and rates and cell

211   infiltration were implemented as described earlier (Notermans et al. 2021c). Tendon-, cartilage-

212   and fat-like tissue were produced at the default rate (2%/day), whereas bone-like tissue was

213   produced at 1.2%/day (similar to the implementation in Isaksson et al. (2006a)). Tendon

214   production in the mechanoregulatory algorithms based on principal strain with (PE-OXY) or

215   without oxygen (PE) was based on a strain-regulated production law (Online Resource 4)

216   (Notermans et al. 2021b) (Notermans et al. 2021c), that predicts an initial increase of tissue

217   production with increasing strain. However, for principal strains over 15%, tissue production

218   decreases with increasing strain. For all models, during the first five days of healing, a baseline

219   tissue production rate (50% of daily production) was assumed to be driven by acute

220   inflammation. After 5 days, the tissue production rate was solely mechanoregulated (Notermans

221   et al. 2021b). For all models, cell infiltration from the extrinsic compartment of the callus was

222   considered (Notermans et al. 2021c) (Fig 2; Online Resource 1 and 5). The cell infiltration rate

223   was set to reach 95% cell density after 2 weeks. The local tissue production in an element in

224   the callus was linearly dependent on the local cell density such that no tissue production occurs

225   if there are no cells present, regardless of the mechanical cue, and mechanoregulated tissue

226   production is allowed fully if the local cell density is 100%. Degradation of tissue was also

227   considered in all models. Namely, as one tissue type is produced, other tissues are degraded at

228   the production rate of the tissue type that is produced.

229

230   **2.4 Material properties for different tissues**

231   To describe the material properties of fat-, tendon-, cartilage- and bone-like tissue, a tissue type-

232   dependent material behaviour was implemented. Scaling coefficients were used to adapt the

233   material behaviour for the different tissue types compared to tendon material properties that

234   were determined in intact tendon (Notermans et al. 2019). The scaling coefficient for fat tissue

11

235 (0.5) was implemented to ensure a decrease in stiffness for fat-like tissue, compared to tendon-

236 like tissue, following Burke et al. (2012). The scaling coefficients for cartilage- and bone-like

237 tissue (2.62, 40.40) were implemented to ensure that the cartilage- and bone-like tissue are 50

238 and 500 times stiffer than tendon tissue at 2N load according to an earlier computational

239 framework for predicting tissue differentiation and formation in bone healing (Isaksson et al.

240 2006a). The material properties were then implemented according to:

241 $$M_{\text{tissue}}^{Callus} = (0.5 * \rho^F + \rho^T + \rho^C * 2.62 + \rho^B * 40.40) * M_{\text{Tendon}}^{intact} \text{ for M} = E_1, E_2, K_1, K_2, E_p, E_n, G_{pn}$$

242 where the material parameter (M) in the healing callus depends on the local fat (ρ^F), tendon

243 (ρ^T), cartilage (ρ^C) and bone (ρ^B) density. We scaled all stiffness parameters in our constitutive

244 material model (Khayyeri et al. 2016; Notermans et al. 2019), for both the collagen

245 (E_1, E_2, K_1, K_2) and ground substance (E_p, E_n, G_{pn}).

246

2.5 Reorientation

248 In each iteration of the healing framework, the collagen fibrils (13/material point with random

249 initial orientation) in the callus were rotated in the direction of the maximum principal strain

250 (Notermans et al. 2021b; Tanska et al. 2018; Wilson et al. 2006) (Notermans et al. 2021c). The

251 fibril reorientation from random to longitudinal alignment was set to occur in four weeks

252 (Notermans et al. 2021b) (Notermans et al. 2021c).

253

2.6 Endochondral bone formation

255 The different mechanobiological algorithms assumed that bone-like tissue formation depends

256 on local mechanical stimuli or the presence of blood supply. In addition to these requirements,

257 the effect of limiting bone formation to endochondral bone formation was investigated (Lin et

al. 2010), i.e. that bone can only form through ossification of cartilage or further ossification/apposition of existing bone. This process was investigated using the principal strain model (referred to as PE-ENDO). The implementation limited bone-like tissue formation to only occur if the two following requirements were met:

- (Maximum) principal strain < 2% ,
- Current density of cartilage ($\rho^C > \rho^C_{endo}$) <u>OR</u> bone ($\rho^B > 0\%$) density,

where two different threshold values for the cartilage density ($\rho^C_{endo} = 20$ or 25%) were explored (referred to as PE-ENDO 20% or PE-ENDO 25%).

2.7 Angiogenesis and oxygen framework

Diffusion simulations for angiogenesis and oxygen were performed every iteration of healing, similarly to an existing framework for oxygen-dependent bone healing (Burke and Kelly 2012). At the first iteration of healing, the callus was deprived of blood vessels and oxygen (angiogenesis and oxygen density was 0%). Every iteration of the healing framework (~1 day), angiogenesis and oxygen diffusion was allowed to occur from the external surface into the healing callus (Online Resource 1 and 5) Angiogenesis and oxygen diffusion were modeled using Darcy's law for diffusion according to:

$$\frac{d\rho}{dt} = D\nabla^2\rho$$

with diffusion constant (D) and density (ρ) (Burke and Kelly 2012; Isaksson et al., 2008). Angiogenesis then occurred in elements where the average octahedral shear strain was lower than a threshold value (A-OSS) (Burke and Kelly 2012; Simon et al. 2011). A node with more than 90% angiogenesis, was considered a matured blood vessel that provided blood supply, and thus this node was a new source for oxygen. In addition, bone-, fat- and tendon-like tissue were

281   allowed to form at these established blood supplies. Additionally, cells were able to consume

282   oxygen (maximum 50% oxygen was consumed at 100% cell density, C=0.5) according to:

283    $$\frac{d\rho^{oxygen}}{dt} = O\nabla^2\rho^{oxygen} - C * \rho^{cells} * \rho^{oxygen}$$

284   with the diffusion constant (O), oxygen density (ρ^{oxygen}), tuning parameter for cell-dependent

285   oxygen diffusion (C) and cell density (ρ^{cells}). The predicted angiogenesis and oxygen

286   distributions affected the tissue formation according to Table 1. To determine how sensitive the

287   predicted tissue distributions were with regards to different angiogenesis- and oxygen-related

288   parameters, a parameter sensitivity analysis was performed, varying the diffusion constant for

289   angiogenesis (A = 0.25 – 0.5 – 1.0) and oxygen (O = 0.25 – 0.5 – 1.0), the extent of cellular

290   oxygen-consumption (C = 0.25 – 0.5 – 0.75) and the octahedral shear strain-threshold for

291   angiogenesis (A-OSS = 3 – 6 – 12%).

292

293   2.8 Healing predictions

294   A total of six mechanobiological algorithms were investigated (Fig 3). From each simulation,

295   the predicted temporal and spatio-temporal evolution of tendon, fat-, cartilage- and bone-like

296   tissue density was characterized throughout 20 weeks of tendon healing and compared to a

297   range of literature findings. Furthermore, the temporal evolution of stiffness at 2N was

298   calculated and compared to experimental data from intact (Khayyeri et al. 2017) and healing

299   (Khayyeri et al. 2020) rat Achilles tendon. Predicted bone tissue formation was validated

300   against in-house measurements of bone-like tissue during rat Achilles tendon healing

301   (Pierantoni et al. 2022). To determine the absolute volumes of bone-like tissue throughout

302   healing, tissue volumes were segmented from 3D tomography data (phase contrast enhanced

303   x-ray microtomography at the Diamond-Manchester Imaging Branchline I13–2) from healing

304   rat Achilles tendon at 1, 3, 12 and 20 weeks of healing (n=3 at each time point). The volume

305 of interest for this quantification was the whole tendon, including both the healing callus and

306 the tendon stumps. To determine the bone-like tissue volume in the simulations, we integrated

307 the element-level bone density multiplied by element volume, for all elements in the callus.

308
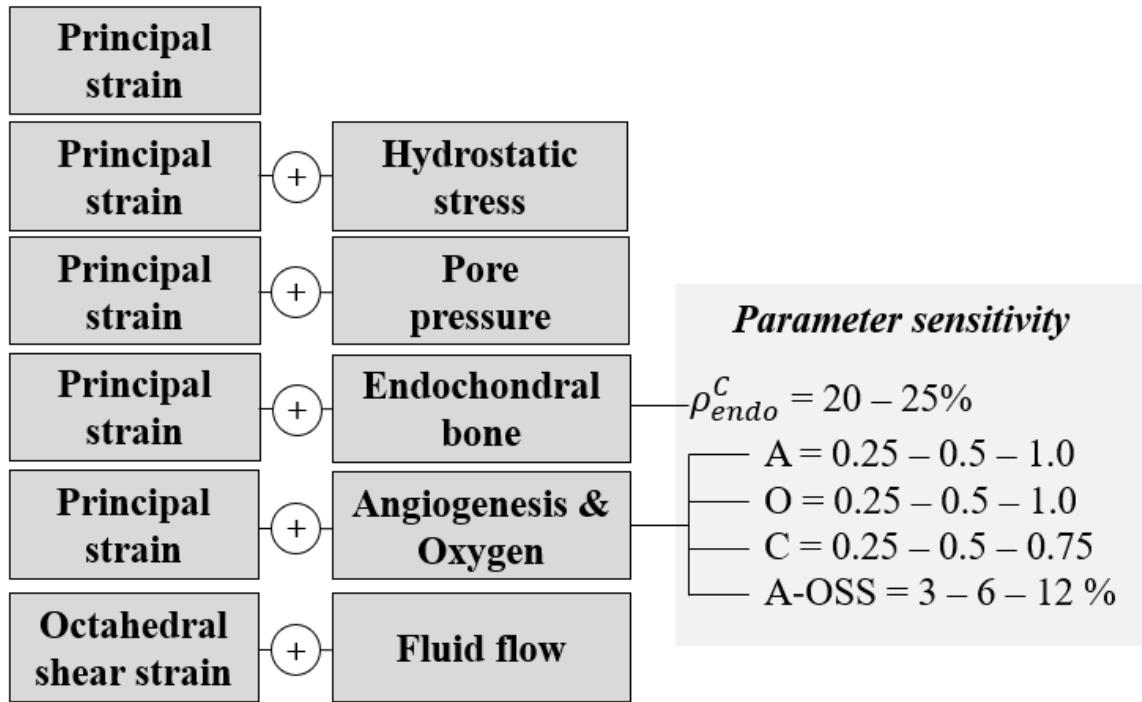
309

310 **Fig 3** *Overview of the six different mechanoregulatory frameworks investigated in this study*

311 *and an overview of the parameter sensitivity analysis for the threshold of endochondral bone*

312 *formation (ρ_{endo}^{C}), diffusion constants for simulations of angiogenesis (A), oxygen diffusion (O)*

313 *and cell-dependent oxygen consumption O. The different algorithms are referred to with these*

314 *abbreviations: Principal strain (PE), principal strain and hydrostatic stress (PE-HS), principal*

315 *strain and pore pressure (PE-PP), principal strain and oxygen (PE-OXY), principal strain with*

316 *endochondral bone formation (PE-ENDO), Octahedral shear strain and fluid flow (OSS-FF).*

317

318

3. Results

This section presents the results of all mechanobiological mechanisms presented in Table 1 (PE, PE-HS, PE-PP, PE-OXY, OSS-FF), and the results predicted when limiting bone formation to the endochondral pathway (PE-ENDO) compared to the default strain model (PE). Finally, the parameter analysis of the strain- and oxygen-dependent algorithm (PE-OXY) is presented.

3.1 Temporal evolution of tissue formation and mechanical properties

The implemented mechanobiological algorithms predicted a unique sequential evolution of tendon-, cartilage- and bone-like tissue formation throughout the first 20 weeks of healing (Fig 4). All algorithms predicted formation of tendon tissue initially, and ended with predicting a significant amount of bone-like tissue formation. The octahedral shear strain and fluid flow stimulus (OSS-FF) predicted a shorter tendon-production phase, and earlier prediction of bone-like tissue formation. On the other hand, the principal strain and oxygen stimulus (PE-OXY) predicted formation of tendon-like tissue for a longer time period. It was also the latest to predict formation of bone-like tissue.

Cartilage-like tissue formation was less prominent than the formation of tendon- or bone-like tissue. Principal strain combined with hydrostatic stress (PE-HS) or pore pressure (PE-PP) predicted slow but gradual cartilage-like tissue production that persisted throughout 20 weeks of healing. On the other hand, the other biophysical stimuli (PE, PE-OXY, OSS-FF) predicted cartilage-like tissue production over a short time span. No fat production was predicted by the principal strain and oxygen stimulus (PE-OXY).

With the progressive formation of tendon-, cartilage- and bone-like tissue, the stiffness of the healing tendon increased throughout healing (Fig 4). The principal strain and oxygen stimulus (PE-OXY) predicted the latest onset of bone-like tissue formation, and therefore it also predicted the slowest stiffness evolution. Yet, the predicted stiffness in this model was within the range of the experimental data during the first weeks of healing and reached intact levels of stiffness at 20 weeks of healing. The other algorithms (PE, PE-HS, PE-PP, OSS-FF) predicted that the stiffness would reach intact levels earlier, i.e. after four to twelve weeks of healing. After reaching intact level of stiffness, the stiffness evolution flattened in an asymptotic fashion.
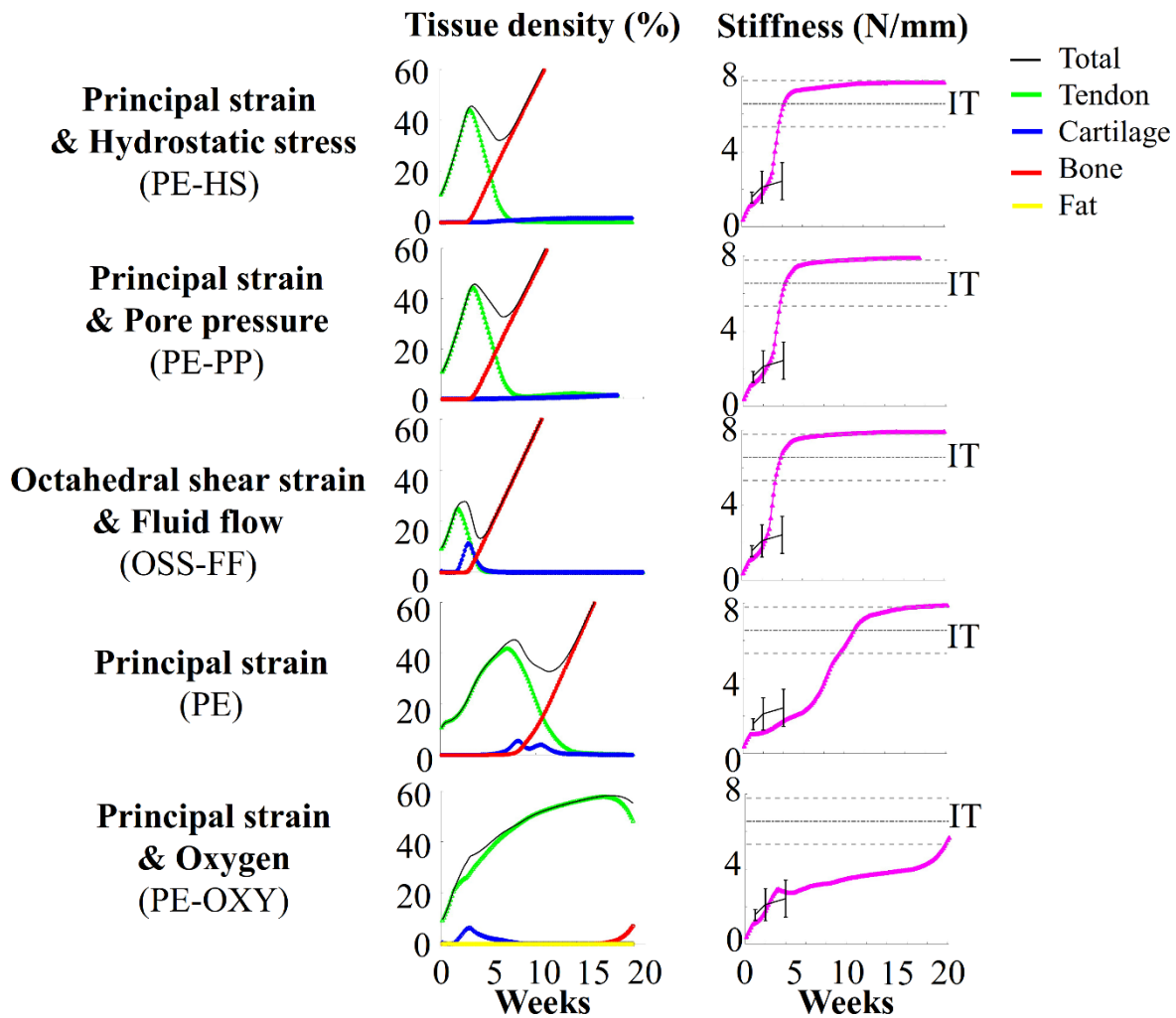
Fig 4 *Temporal evolution of tendon-, cartilage-, fat- and bone-like density and stiffness throughout 20 weeks of healing. Stiffness data is compared to experimental data (black lines, mean ± standard deviation) from intact (IT) (Khayyeri et al. 2017) and healing rat Achilles tendons subjected to free cage activity loading at 1, 2 and 4 weeks (Khayyeri et al. 2020).*

3.2 Spatial evolution of tissue formation

All mechanobiological algorithms predicted heterogeneous tissue formation throughout 20 weeks of healing (Fig 5). During the initial phase of tendon formation, the production was initially higher in the callus periphery compared to the callus core. This was followed by a homogeneous production of cartilage-like and bone-like tissue. The principal strain and oxygen stimulus (PE-OXY) predicted the longest production of tendon tissue. This algorithm also showed the most heterogeneous tendon formation with high tendon content in the periphery for at least 10 weeks. Tendon density disappeared quickest in the simulations with octahedral shear strain and fluid flow (OSS-FF) as the regulatory stimulus.

Also, the spatial mapping of the density evolution display that cartilage-like tissue production is less prominent than either tendon- or bone-like tissue production for all stimuli. Yet, principal strain and oxygen (PE-OXY) predicted the highest content of cartilage-like tissue in the callus core. On the other hand, the principal strain and pore pressure (PE-PP) stimulus predicted long term cartilage-like tissue production at the stump interface. Principal strain alone (PE) or with hydrostatic stress (PE-HS) predicted small regions of cartilage-like tissue production next to the tendon stumps in the periphery.

375　As mentioned above, all mechanobiological algorithms predicted formation of bone-like tissue.

376　Bone-like tissue was generally first formed in the periphery of the callus, before spreading to

377　the callus core and throughout the whole callus. Yet, for the principal strain and oxygen

378　stimulus (PE-OXY), bone-like tissue formation was predicted rather late and did not spread to

379　the whole callus by 20 weeks.

380

381
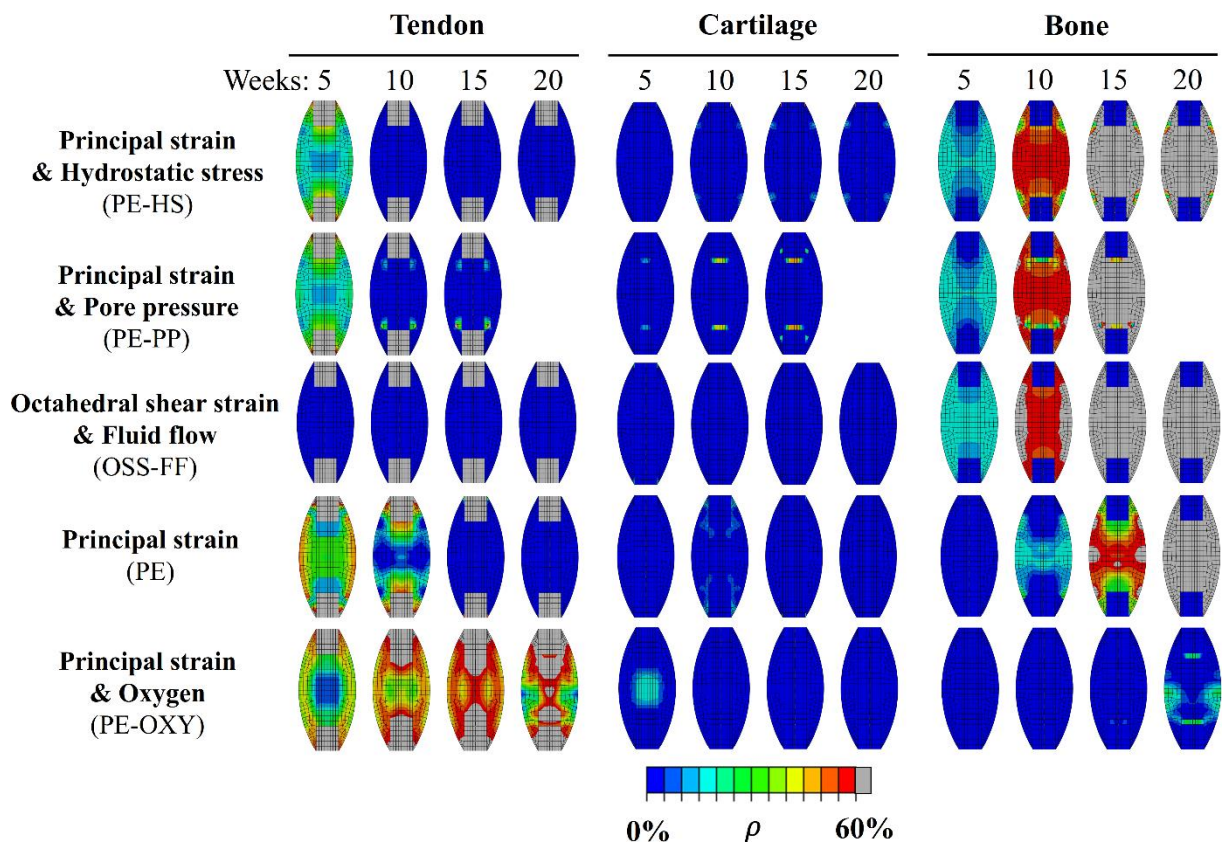
382　*Fig 5 Spatio-temporal evolution of tendon-, cartilage- and bone-like tissue density (ρ) at 5, 10,*

383　*15 and 20 weeks of healing.*

384

385　**3.3 Endochondral bone formation**

386　Exploring the effect of adding the requirement that bone-like tissue could only form through

387　the endochondral pathway in the principal strain model (PE-ENDO 20% and 25%) decreased

the predicted bone-like tissue content. Instead, more persistent tendon- and cartilage-like tissue

formation was predicted, compared to the default principal strain model (PE) that did not limit

bone-like tissue formation to the endochondral pathway (Fig 6).
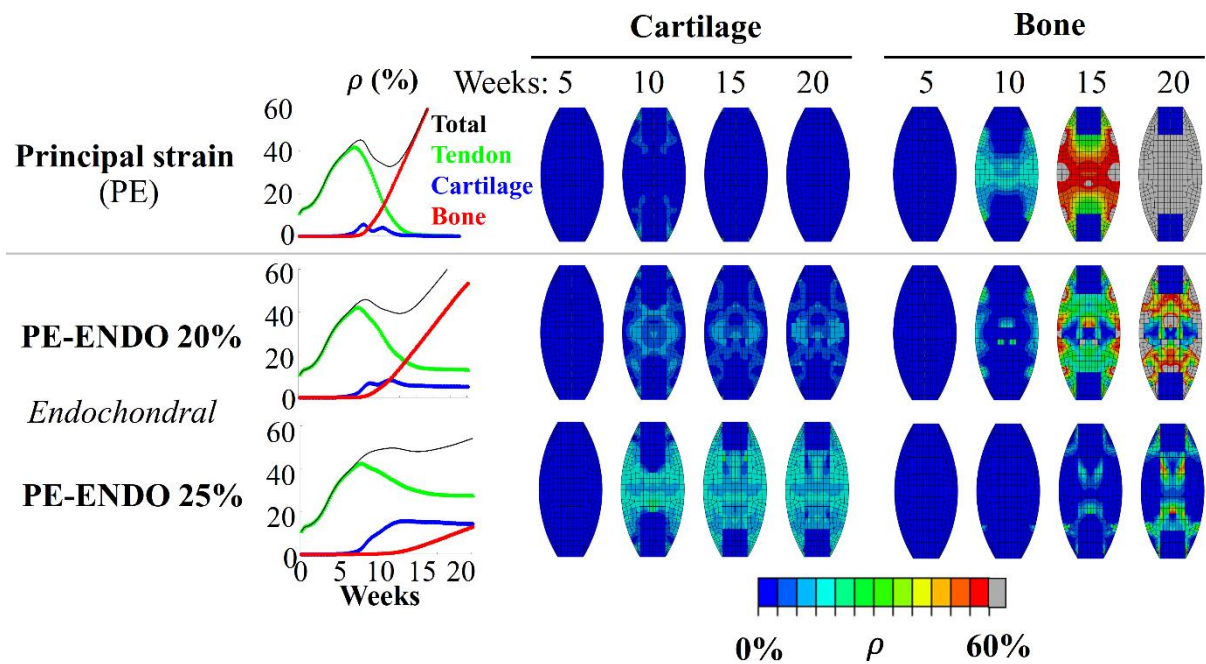
Fig 6 *Effect of limiting bone formation to the endochondral pathway for the principal strain*

(PE) stimulus. Spatio-temporal predictions of tendon-, cartilage- and bone-like tissue density

(ρ) throughout 20 weeks of healing is depicted.

3.4 Parameter sensitivity of the oxygen framework

The parameter sensitivity study for the principal strain and oxygen framework (PE-OXY)

showed large variations in the predictions of temporal tendon-, cartilage-, bone- and fat-like

tissue formation throughout the 20 weeks of healing (Fig 7). Parameter perturbations that

increased the process of angiogenesis or oxygen concentration (C = 0.25, A-OSS = 12%, O =

1.0, A = 1.0), generally predicted decreased formation of cartilage, whereas all perturbations

that created more hypoxic conditions (C = 0.75, A-OSS = 3%, O = 0.25, A = 0.25), predicted

404   increased formation of cartilage. Increased bone-like tissue content was predicted using

405   different parameter perturbations that both increased and decreased angiogenesis and oxygen

406   levels. Fat tissue was only predicted to form in one simulation case (A-OSS = 12%).

407
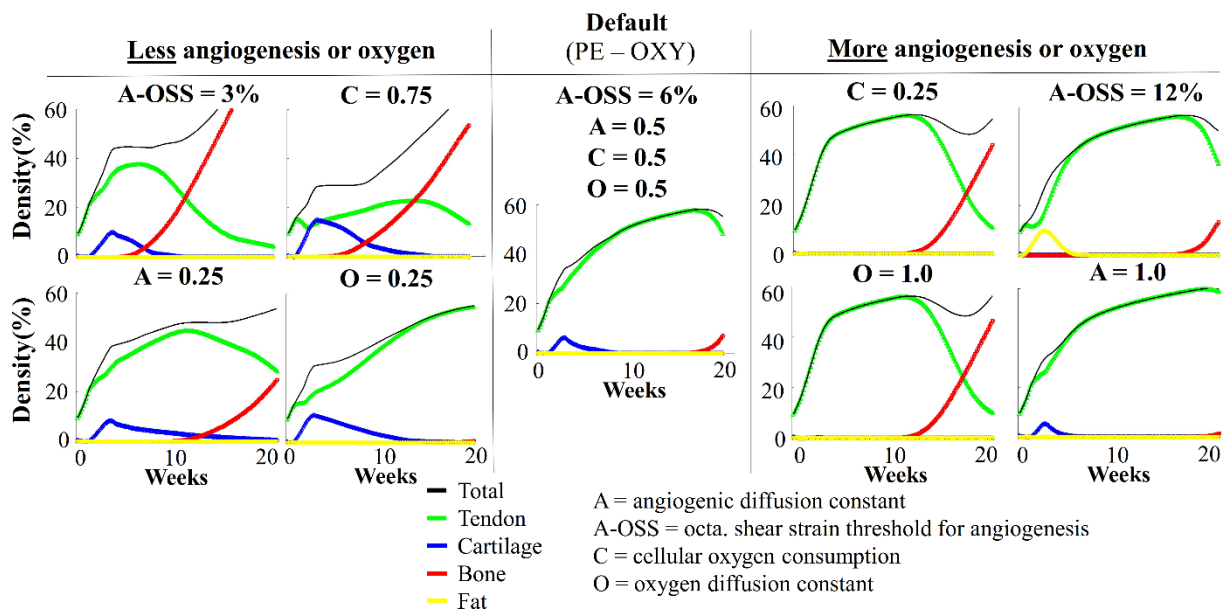
409   *Fig 7 Parameter sensitivity analysis for the principal strain and oxygen framework (PE-OXY).*

410   *The temporal evolution of the tendon-, cartilage-, bone- and fat-like tissue density, throughout*

411   *the first 20 weeks of healing.*

412

413   The temporal evolution of the volume of bone-like tissue in the healing callus was compared to

414   in-house quantitative measurements of the total volume of bone-like tissue in healing rat

415   Achilles tendon subjected to free cage activity at 1, 3, 12 and 20 weeks of healing

416   (N=3/timepoint) (Figure 8) (Pierantoni et al. 2022). Most of the mechanobiological algorithms

417   overpredicted the bone volume grossly, whereas the algorithms based on principal strain

418   combined with oxygen (PE-OXY) or the principal strain combined with endochondral (PE-

ENDO 25%) pathway mostly predicted the experimentally observed bone formation after 20 weeks of healing.
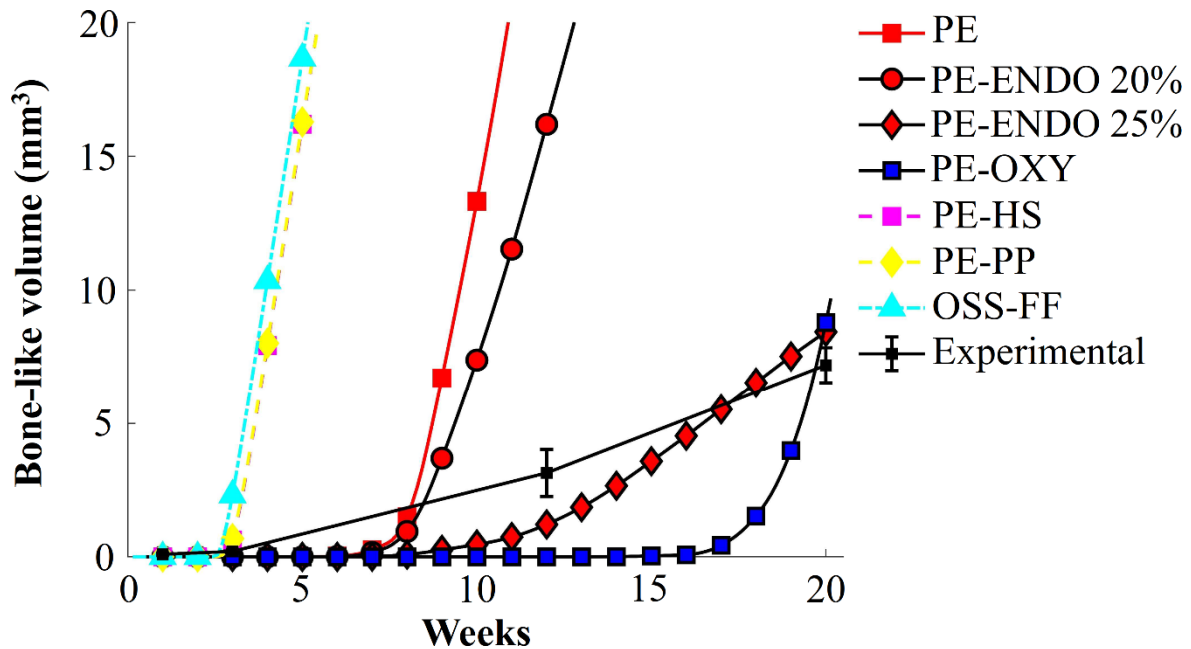
Fig 8 Temporal evolution of the bone volume for the different biophysical stimuli versus in-house experimental data (mean ± standard deviation, N=3/timepoint) from healing rat Achilles tendon, subjected to free cage activity (Pierantoni et al. 2022). Experimental data was assessed at 1, 3, 12 and 20 weeks of healing.

4. Discussion

In this study we present the development of the first computational framework investigating mechanobiological processes regulating formation of multiple tissue types during tendon healing. Specifically, we incorporated mechanical, cellular, angiogenesis and oxygen-related stimuli to predict heterogeneous tissue production, organization and mechanical properties during tendon healing. Different biophysical stimuli, e.g. principal strain, hydrostatic stress,

434 pore pressure, octahedral shear strain and fluid flow, angiogenesis and oxygen concentration

435 were considered, according to earlier work in bone healing (Burke and Kelly 2012; Isaksson et

436 al. 2006a; Isaksson et al. 2008). The different biophysical stimuli displayed the capability to

437 reproduce different experimental observations of spatial and temporal evolution of tendon, fat-

438 , cartilage- and bone-like tissue during tendon healing in small animal studies.

439

440 Overall, the different biophysical stimuli predicted tissue production pathways roughly similar

441 to experimental observations with predominantly tendon production throughout the first month

442 of healing, followed by formation of cartilage-like regions and eventually predicting significant

443 formation of bone-like regions. Tendon production was higher in the periphery since cell

444 infiltration from the extrinsic compartment allowed early tendon production in the periphery

445 whereas the tendon core (lacking cells) could not produce tissue. However, several of the

446 biophysical stimuli predicted too fast and too much bone formation (Fig 8).

447

448 Temporally, one experimental study showed a decrease in tendon phenotype (less collagen type

449 1) and increase in cartilage-like phenotype (more collagen type 2) throughout 17 weeks of

450 healing (da Silva et al. 2020). This exemplifies the decrease in tendon-like phenotype

451 throughout time, as observed in most of our healing simulations. Yet, the experimental data

452 also imply long term presence of cartilage-like regions, and it was also shown that bone-like

453 regions are surrounded by cartilage-like regions (Darrieutort-Laffite et al. 2019). Only the

454 models with the principal strain and hydrostatic stress (PE-HS) or pore pressure (PE-PP)

455 stimuli, and the principal strain with endochondral bone formation models (PE-ENDO), were

456 able to predict long term presence of cartilage.

457

458   Spatially, the different biophysical stimuli predicted rather small areas of cartilage-like tissue

459   formation. This agrees qualitatively with experimental studies, as most studies observe rather

460   small concentrated patches of proteoglycans (da Silva et al. 2020; Howell et al. 2017; Korntner

461   et al. 2017; Misir et al. 2019). Different studies found cartilage-like staining (Korntner et al.

462   2017) and cells (Khayyeri et al. 2020) near the tendon stump. Howell et al. (2017) observed

463   stronger proteoglycan staining towards the periphery and Khayyeri et al. (2020) also described

464   more isolated islands of cartilage-like cells throughout the healing callus. Most of these spatial

465   findings were predicted using the different algorithms.

466

467   In terms of bone-like tissue formation, experimental studies identified bone-like regions by 5-

468   16 weeks of healing (Asai et al. 2014; Chen et al. 2017; Howell et al. 2017; Huber et al. 2020;

469   Lin et al. 2010; Zhang et al. 2016). In alignment with these experimental results, the octahedral

470   shear strain and fluid flow (OSS-FF), principal strain combined with hydrostatic stress (PE-HS)

471   and pore pressure (PE-PP) algorithms predicted bone formation as early as four weeks of

472   healing. Also, our models predicted large bone volumes in the whole callus, as observed

473   experimentally at 15 (Sakabe et al. 2018) and 16 weeks (Hsieh et al. 2016) (Fig 1). Yet, also

474   the experimental studies show high variations in the locations and sizes of the different bone-

475   like regions, and more experimental data would be valuable for further development and

476   validation of the computational framework.

477

478   Throughout our study, we observed a high sensitivity of the healing predictions to the chosen

479   parameters. One example is the production rate of tendon for the different stimuli. The principal

480   strain stimulus, with (PE-OXY) or without oxygen (PE), predicted tendon formation according

481   to the strain-regulated production law with a maximum production rate of (2%/day), similar to

482 our recent healing frameworks (Notermans et al. 2021b) (Notermans et al. 2021c). However, a

483 constant production rate of 2%/day was used for the older mechanoregulatory models (PE-HS,

484 PE-PP, OSS-FF). Consequently, the tendon density and stiffness evolved quicker in the older

485 mechanoregulatory models, compared to the principal strain (PE) and oxygen (PE-OXY)

486 stimulus, which were implemented more similarly to our recently developed healing

487 framework. The slower recovery of stiffness for the strain (and oxygen) stimulus also

488 contributed to slower evolution of bone production, since it took a longer time for strains to

489 drop below the threshold value for bone formation (2%). The effect of the production rates is

490 also reflected in the quantitative comparison of the temporal evolution of the total bone volume

491 predicted in our frameworks with in-house experimental data (Fig 8). Thus, most models

492 overpredicted the volume of bone-like tissue throughout the simulation, when comparing to the

493 in-house experimental data. Using the strain-regulated production law for tendon (PE, PE-

494 OXY), particularly in combination with allowing only endochondral bone formation (PE-

495 ENDO), predicted bone formation at a more similar rate to the experimental data than the older

496 mechanoregulatory models. Yet, the default principal strain and oxygen stimulus (PE-OXY)

497 still underpredicted the experimentally observed bone formation, but as indicated by the

498 parameter analysis (Fig 8), the predicted bone formation varies greatly with a large number of

499 unknown parameters. Note that quantitative bone volumes from experimental data (Fig. 8)

500 include bone-like volumes in the intact tendon stumps. This probably means that the presented

501 data overestimates the bone-like tissue volume inside the healing callus. Elaborate data for

502 validation should be used to calibrate parameters, such as the production rates of the different

503 tissue types. Even though many model parameters need further characterization and validation,

504 the current framework clearly shows, as a proof-of-concept, that this computational framework

505 can be an important tool in understanding tendon mechanobiology during healing. Particularly,

506 when trying to understand mechanobiological mechanisms of tissue differentiation or the

507 formation of different tissue types during tendon healing.

508

509 We explored the effect of allowing only endochondral bone formation in combination with the

510 principal strain modulus (PE-ENDO), as this has been proposed to be the main pathway of

511 heterotopic ossification during Achilles tendon healing (Lin et al. 2010). Interestingly, this led

512 to an increased production and persistence of tendon and cartilage, whereas it limited the

513 predicted bone formation, compared to the default strain model. These results agreed better

514 with the quantitative bone-volumes in Fig 8. Additionally, these models predicted experimental

515 observations of long term (>15 weeks) presence of cartilage-like tissue (da Silva et al. 2020) in

516 co-existence with more isolated islands of bone-like tissue (Darrieutort-Laffite et al. 2019),

517 instead of a fully ossified callus without any cartilage-like tissue present. This last result

518 highlights that modeling the endochondral bone formation process may be critical to predict

519 reasonable cartilage- and bone-like tissue formation during tendon healing.

520

521 We also investigated a mechanobiological algorithm that combined mechano-regulation with

522 predictions of oxygen and angiogenesis (PE-OXY) (Burke and Kelly 2012). In short, this model

523 considered the ingrowth of blood vessels which provides oxygen to the healing callus from the

524 periphery into the hypoxic tendon core (Online Resource 5). This framework shifted the

525 cartilage-like tissue formation to the tendon core, as it is deprived of oxygen during early

526 healing and cartilage production occurs under hypoxic conditions (Lin et al. 2010). On the other

527 hand, blood vessel formation (through angiogenesis) has been found in bone-like areas in

528 tendon (Darrieutort-Laffite et al. 2019). The default parameters used for the principal strain and

529 oxygen framework (PE-OXY) predicted bone formation at a late stage of healing (>15 weeks)

530 and potentially underpredicted the amount of bone formation observed in experimental data.

531 Yet, the parameter sensitivity analysis identified large variations in the temporal prediction of

532 fat-, cartilage- and bone-like tissue formation with changes in different parameters that remain

533 uncertain. Experimental measurements of spatial and temporal evolution of oxygen

534 concentrations and blood vessel formation will be important to enable validation of these

535 frameworks, similar to the validation in the bone healing framework (Burke and Kelly 2012).

536 Only one healing model (A-OSS = 12%) predicted the production of fat tissue, and fat

537 production was predicted during the first weeks of healing. This agrees with Khayyeri et al.

538 (2020) that found fat-like cells during the first weeks of healing. We implemented a principal

539 strain threshold for fat-like tissue prediction of 25%, and material properties that scaled all

540 constitutive material properties by 0.5, compared to tendon. Both, the strain threshold and

541 material properties for the fat-like tissue lack experimental validation, and should be addressed

542 in the future.

543

544 One limitation of our current framework is that the experimental data for cartilage-like

545 (proteoglycan and collagen staining) and bone-like tissue formation (x-rays or μCT) shows

546 multiple, unconnected, localized and discretized areas of chondrification and ossification. Yet,

547 the finite element modeling approach uses continuum mechanics, which has the inherent effect

548 that ossified areas are fully integrated and connected to adjacent tissue, whereas it may be

549 possible that these ossified areas are not fully integrated in the surrounded matrix. Future in situ

550 imaging techniques may characterize the heterogeneous strain distribution around ossifications

551 and may quantify the loadbearing of these ossifications. This type of imaging experiments may

552 be key to determine the role of these ossifications on overall tendon mechanics, heterogeneous

553 mechanical stimuli, and mechanisms of tendon failure.

554

555   In this study, we developed a mechanobiological tendon healing framework to predict tissue

556   differentiation during tendon healing types based on mechanoregulatory schemes in literature.

557   A wide range of biophysical stimuli, including purely mechanical stimuli but also cell

558   infiltration, angiogenesis and oxygen concentration were explored to govern the formation of

559   tendon-, fat-, cartilage- and bone-like tissue throughout the first months of tendon healing.

560   Different biophysical stimuli captured specific aspects of experimentally observed features.

561   Specifically, we predicted experimental observations of heterogeneous tissue formation and

562   showed that mechanobiology may play a role in governing tissue formation and tissue

563   differentiation during healing. This study provides the first numerical tool to investigate

564   mechanobiological mechanisms governing the formation of tendon and other tissue types

565   during tendon healing. Further development and validation of this model are necessary when

566   more spatial and temporal experimental data is available, yet this framework can aid in

567   designing better rehabilitation protocols after tendon rupture.

568

569

570

References

Asai S et al. (2014) Tendon Progenitor Cells in Injured Tendons Have Strong Chondrogenic
     Potential: The CD 105-Negative Subpopulation Induces Chondrogenic Degeneration
     Stem cells 32:3266-3277

Buckley CT, Vinardell T, Kelly DJ (2010) Oxygen tension differentially regulates the
     functional properties of cartilaginous tissues engineered from infrapatellar fat pad
     derived MSCs and articular chondrocytes Osteoarthritis and Cartilage 18:1345-1354

Burke DP, Kelly DJ (2012) Substrate stiffness and oxygen as regulators of stem cell
     differentiation during skeletal tissue regeneration: a mechanobiological model PloS
     one 7:e40737

Carter DR, Beaupré GS, Giori NJ, Helms JA (1998) Mechanobiology of skeletal regeneration
     Clinical Orthopaedics and Related Research (1976-2007) 355:S41-S55

Checa S, Byrne DP, Prendergast PJ (2010) Predictive modelling in mechanobiology:
     combining algorithms for cell activities in response to physical stimuli using a lattice-
     modelling approach. In: Computer methods in mechanics. Springer, pp 423-435

Chen G, Jiang H, Tian X, Tang J, Bai X, Zhang Z, Wang L (2017) Mechanical loading
     modulates heterotopic ossification in calcific tendinopathy through the mTORC1
     signaling pathway Molecular medicine reports 16:5901-5907

Claes L, Heigele C (1999) Magnitudes of local stress and strain along bony surfaces predict
     the course and type of fracture healing Journal of biomechanics 32:255-266

da Silva FS, Abreu BJ, Eriksson BI, Ackermann PW (2020) Complete mid-portion rupture of
     the rat achilles tendon leads to remote and time-mismatched changes in uninjured
     regions Knee Surgery, Sports Traumatology, Arthroscopy:1-10

594   Darrieutort-Laffite C et al. (2019) Rotator Cuff Tenocytes Differentiate into Hypertrophic

595   Chondrocyte-Like Cells to Produce Calcium Deposits in an Alkaline Phosphatase-

596   Dependent Manner Journal of Clinical Medicine 8:1544

597   El-Akkawi AI, Joanroy R, Barfod KW, Kallemose T, Kristensen SS, Viberg B (2018) Effect

598   of Early Versus Late Weightbearing in Conservatively Treated Acute Achilles Tendon

599   Rupture: A Meta-Analysis The Journal of Foot and Ankle Surgery 57:346-352

600   doi:https://doi.org/10.1053/j.jfas.2017.06.006

601   Freedman BR, Bade ND, Riggin CN, Zhang S, Haines PG, Ong KL, Janmey PA (2015) The

602   (dys) functional extracellular matrix Biochimica Et Biophysica Acta (BBA)-Molecular

603   Cell Research 1853:3153-3164

604   Ganestam A, Kallemose T, Troelsen A, Barfod KW (2016) Increasing incidence of acute

605   Achilles tendon rupture and a noticeable decline in surgical treatment from 1994 to

606   2013. A nationwide registry study of 33,160 patients Knee Surgery, Sports

607   Traumatology, Arthroscopy 24:3730-3737

608   Geris L, Gerisch A, Vander Sloten J, Weiner R, Van Oosterwyck H (2008) Angiogenesis in

609   bone fracture healing: a bioregulatory model Journal of theoretical biology 251:137-

610   158

611   Hausman M, Schaffler M, Majeska R (2001) Prevention of fracture healing in rats by an

612   inhibitor of angiogenesis Bone 29:560-564

613   Hirao M, Tamai N, Tsumaki N, Yoshikawa H, Myoui A (2006) Oxygen tension regulates

614   chondrocyte differentiation and function during endochondral ossification Journal of

615   Biological Chemistry 281:31079-31092

616   Holm C, Kjaer M, Eliasson P (2015) A chilles tendon rupture–treatment and complications: A

617   systematic review Scandinavian journal of medicine & science in sports 25:e1-e10

618   Howell K et al. (2017) Novel model of tendon regeneration reveals distinct cell mechanisms

619   underlying regenerative and fibrotic tendon healing Scientific reports 7:45238

620   Hsieh C-F et al. (2016) Scaffold-free Scleraxis-programmed tendon progenitors aid in

621   significantly enhanced repair of full-size Achilles tendon rupture Nanomedicine

622   11:1153-1167

623   Huber AK et al. (2020) Immobilization after injury alters extracellular matrix and stem cell

624   fate The Journal of clinical investigation 130:5444-5460

625   Huttunen TT, Kannus P, Rolf C, Felländer-Tsai L, Mattila VM (2014) Acute Achilles tendon

626   ruptures: incidence of injury and surgery in Sweden between 2001 and 2012 The

627   American journal of sports medicine 42:2419-2423

628   Isaksson H, Van Donkelaar CC, Huiskes R, Ito K (2006a) Corroboration of

629   mechanoregulatory algorithms for tissue differentiation during fracture healing:

630   comparison with in vivo results Journal of Orthopaedic Research 24:898-907

631   Isaksson H, van Donkelaar CC, Huiskes R, Yao J, Ito K (2008) Determining the most

632   important cellular characteristics for fracture healing using design of experiments

633   methods Journal of Theoretical Biology 255:26-39

634   Isaksson H, Wilson W, van Donkelaar CC, Huiskes R, Ito K (2006b) Comparison of

635   biophysical stimuli for mechano-regulation of tissue differentiation during fracture

636   healing Journal of biomechanics 39:1507-1516

637   Khayyeri H et al. (2017) Achilles tendon compositional and structural properties are altered

638   after unloading by botox Scientific reports 7:13067

639   Khayyeri H et al. (2020) Diminishing effects of mechanical loading over time during rat

640   Achilles tendon healing PloS one 15:e0236681

641 Khayyeri H, Longo G, Gustafsson A, Isaksson H (2016) Comparison of structural anisotropic

642   soft tissue models for simulating Achilles tendon tensile behaviour Journal of the

643   mechanical behavior of biomedical materials 61:431-443

644 Korntner S et al. (2017) A high-glucose diet affects Achilles tendon healing in rats Scientific

645   reports 7:1-12

646 Lacroix D, Prendergast P (2002) A mechano-regulation model for tissue differentiation during

647   fracture healing: analysis of gap size and loading Journal of biomechanics 35:1163-

648   1171

649 Lemme NJ, Li NY, DeFroda SF, Kleiner J, Owens BD (2018) Epidemiology of Achilles

650   tendon ruptures in the United States: athletic and nonathletic injuries from 2012 to

651   2016 Orthopaedic journal of sports medicine 6:2325967118808238

652 Lin L, Shen Q, Xue T, Yu C (2010) Heterotopic ossification induced by Achilles tenotomy

653   via endochondral bone formation: expression of bone and cartilage related genes Bone

654   46:425-431

655 Misir A, Kizkapan TB, Arikan Y, Akbulut D, Onder M, Yildiz KI, Ozkocer SE (2019) Repair

656   within the first 48 h in the treatment of acute Achilles tendon ruptures achieves the

657   best biomechanical and histological outcomes Knee Surgery, Sports Traumatology,

658   Arthroscopy:1-10

659 Notermans T, Hammerman H, Eliasson P, Isaksson H (2021a) Tendon mechanobiology in

660   small-animal experiments during post-transection healing Eur Cell Mater 41:375-391

661   doi:10.22203/eCM.v042a23

662 Notermans T, Khayyeri H, Isaksson H (2019) Understanding how reduced loading affects

663   Achilles tendon mechanical properties using a fibre-reinforced poro-visco-hyper-

664   elastic model Journal of the mechanical behavior of biomedical materials 96:301-309

665   Notermans T, Tanska P, Korhonen RK, Khayyeri H, Isaksson H (2021b) A numerical

666   framework for mechano-regulated tendon healing—Simulation of early regeneration

667   of the Achilles tendon PLOS Computational Biology 17:e1008636

668   Nyyssönen T, Lüthje P, Kröger H (2008) The increasing incidence and difference in sex

669   distribution of Achilles tendon rupture in Finland in 1987–1999 Scandinavian Journal

670   of Surgery 97:272-275

671   Ochen Y et al. (2019) Operative treatment versus nonoperative treatment of Achilles tendon

672   ruptures: systematic review and meta-analysis bmj 364:k5120

673   Palmes D, Spiegel H, Schneider T, Langer M, Stratmann U, Budny T, Probst A (2002)

674   Achilles tendon healing: long-term biomechanical effects of postoperative

675   mobilization and immobilization in a new mouse model Journal of orthopaedic

676   research 20:939-946

677   Pierantoni M et al. (2022) Spatiotemporal and microstructural characterization of heterotopic

678   ossification in healing rat Achilles tendons by 3D phase-contrast enhanced

679   synchrotron micro-tomography. Paper presented at the Orthopeadic Research Society

680   Annual Meeting, Tampa, Florida, USA, 4-8 February 2022

681   Sakabe T et al. (2018) Transcription factor scleraxis vitally contributes to progenitor lineage

682   direction in wound healing of adult tendon in mice Journal of Biological

683   Chemistry:jbc. RA118. 001987

684   Simon U, Augat P, Utz M, Claes L (2011) A numerical model of the fracture healing process

685   that describes tissue development and revascularisation Computer methods in

686   biomechanics and biomedical engineering 14:79-93

687   Song H, Polk JD, Kersh ME (2019) Rat bone properties and their relationship to gait during

688   growth Journal of Experimental Biology 222:jeb203554

689   Tanska P, Julkunen P, Korhonen RK (2018) A computational algorithm to simulate

690   disorganization of collagen network in injured articular cartilage Biomechanics and

691   Modeling in Mechanobiology 17:689-699

692   Wilson W, Driessen N, Van Donkelaar C, Ito K (2006) Prediction of collagen orientation in

693   articular cartilage by a collagen remodeling algorithm Osteoarthritis and Cartilage

694   14:1196-1202

695   Zhang C, Zhang Y, Zhong B, Luo Cf (2016) SMAD 7 prevents heterotopic ossification in a

696   rat Achilles tendon injury model via regulation of endothelial–mesenchymal transition

697   The FEBS journal 283:1275-1285

698